M7: EUV Lab Course Instructions

Content

1. EUV/XUV Radiation and Optics

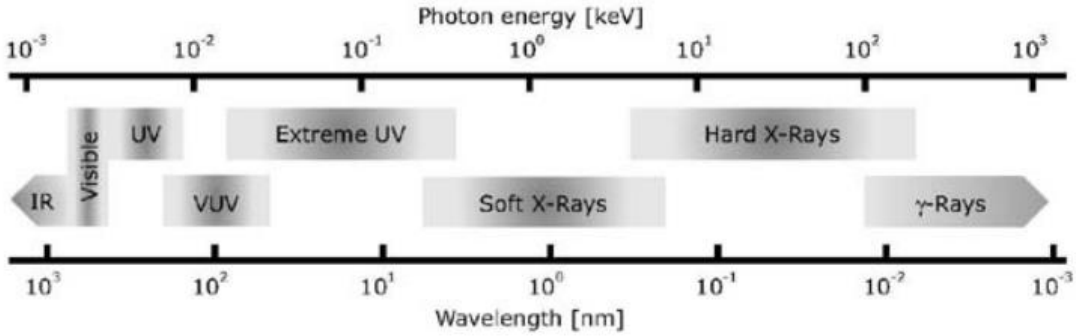

Figure 1. Spectrum of electromagnetic radiation.

Extreme ultraviolet radiation (EUV or XUV) is located in the spectral range between vacuum ultraviolet and soft X-rays. Therefore, as shown in Figure 1, its photon energy extends from 30 eV to 250 eV (spectral range between 5 nm to 40 nm) [1]. The radiation in this specific spectral region is absorbed by most of materials within few tens of nanometers to few micrometers. This historically limited the development of EUV applications. However, with the short wavelength, EUV light has the potential to reveal and modify small structures in applications like microscopy and lithography with resolution down to several nanometers. The strong interaction with matter due to the presence of core level absorption edges of almost every chemical element in the EUV spectral range provides high elemental contrast, which can be employed, for instance, in spectroscopy. Taking into account the recent progress in the development of sources and optics, a multiplicity of EUV applications in the semiconductor industry, thin film technology, life and material sciences is envisioned at present.

Manufacturing integrated circuits (IC) is the driving force for the development of EUV lithography. Presently, deep UV (DUV) radiation at 193 nm (ArF excimer laser) is used for lithography [2]. In order to reduce the size of the nanoelectronic devices even further, advanced lithography technology based on EUV radiation has been developed in the last decade [2]. EUV lithography employs radiation from laser-produced plasma around 13.5 nm wavelength. The plasma is generated by either an intense Nd:YAG or CO_2 laser focused on tin droplets. The emitted EUV radiation is collected and imaged on the reticle, which pattern (an IC) is transferred on the wafer (Fig. 2). Then, the reflected EUV radiation is imaged on the wafer by projection optics. All EUV optics are based on multilayer Bragg mirrors consisting of alternating Si/Mo layers. First EUV lithography scanners are already used for IC production.

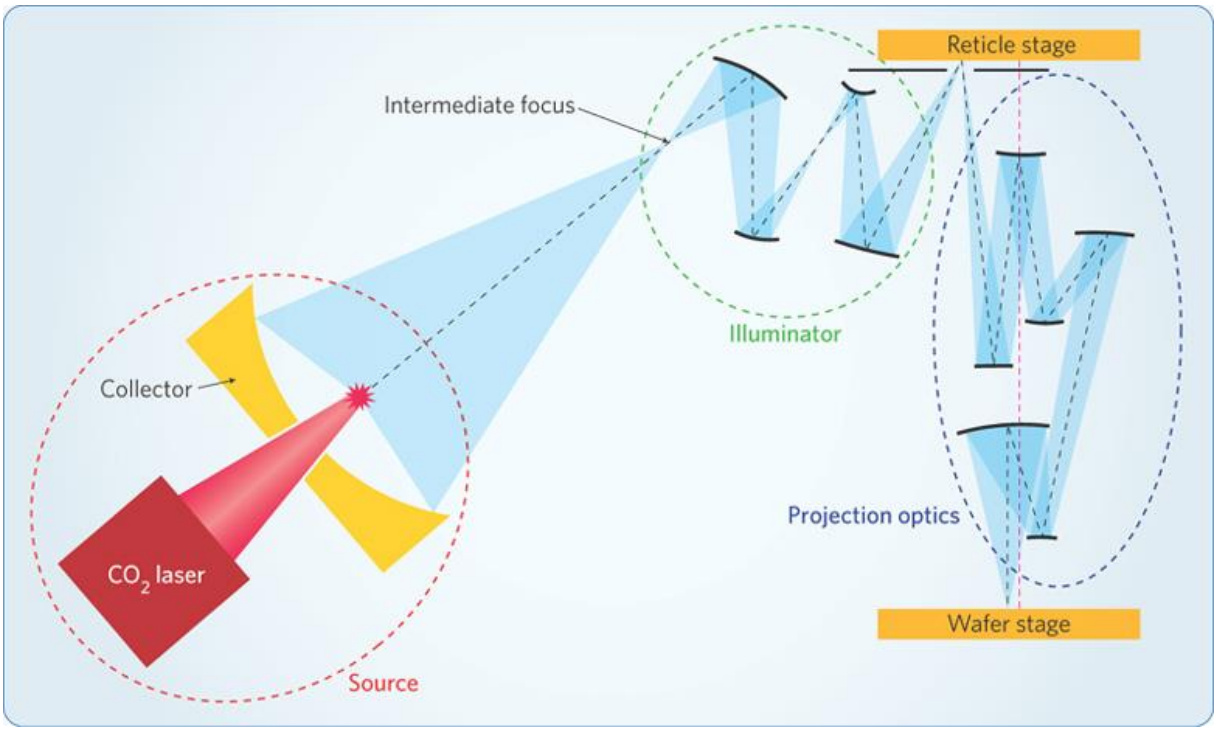

Figure 2. Optical scheme of the scanner used in EUV lithography [2].

EUV Optics

Interaction between electromagnetic radiation and matter is commonly described by the complex index of refraction

$$\tilde{n} = n + ik.$$

Here, the real part of the refractive index n indicates the phase velocity, whereas the imaginary part k indicates the amount of absorption, when the light wave propagates through the material. For X-ray and EUV radiation, the complex refractive index deviates only slightly from unity and usually has a real part smaller than 1. Therefore, it is normally written as

$$n = 1 - \delta + i\beta.$$

At the interface between vacuum and a material, which real part of the refractive index $1 - \delta$ is smaller than 1 (Fig. 3), total external reflection will occur for angle of incidence below a critical angle. For X-ray and EUV optics, the critical angle is measured from the surface of the optic (grazing incidence) and it is typically below 10°, depending on the wavelength and material. The dependence of the reflectivity on the grazing angle for different surface materials is shown in Figure 4.

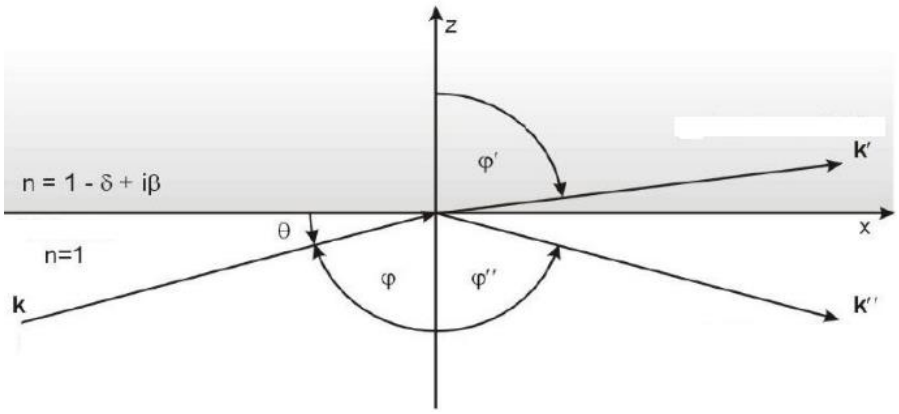

Figure 2. Reflection and refraction of a wave at the interface between vacuum and a material with refractive index n=1- δ+iβ.

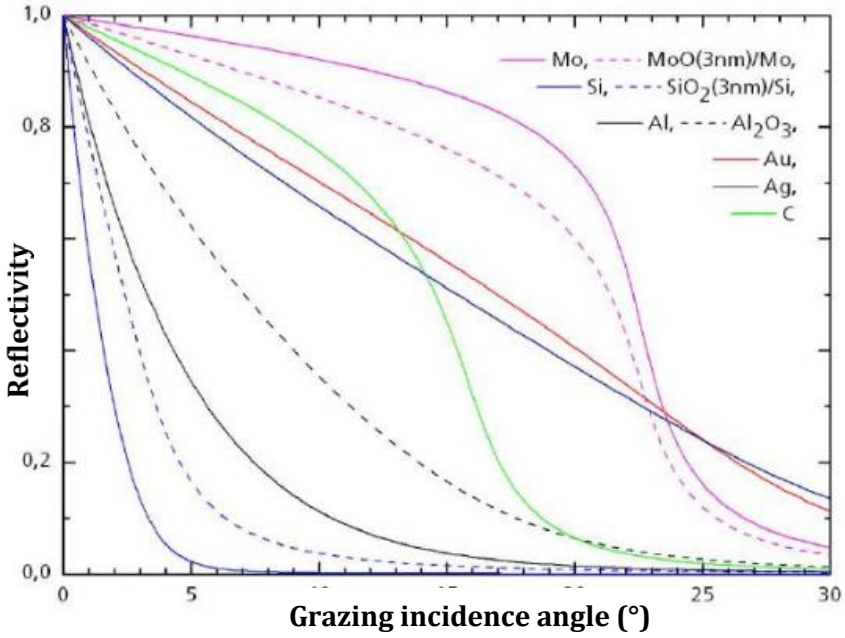

Figure 3. Dependence of the reflectivity of EUV light at 13.5 nm wavelength on the grazing incidence angle (measured from the surface) for different materials.

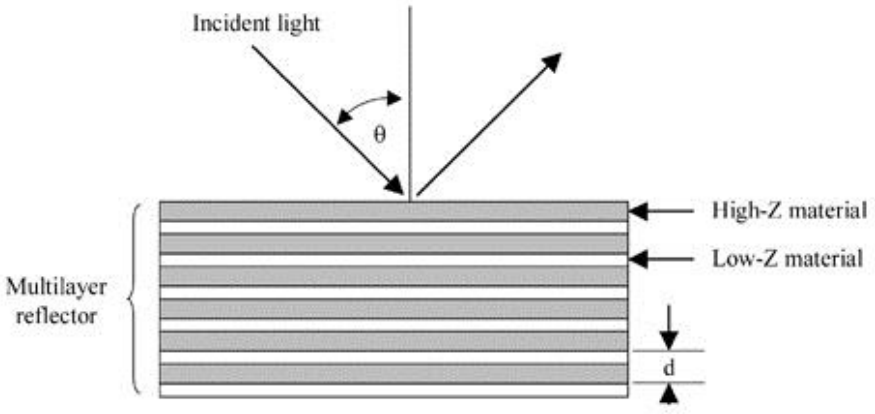

Figure 5. Multilayer structure for efficient reflection of EUV radiation (Bragg mirror).

Another possibility to enhance the reflectivity of EUV radiation is to use multilayer Bragg mirrors. A typical structure of the binary multilayer mirror is shown in Figure 5. Its working principle is based on multiple beam interference of waves partly reflected at many interfaces. The maximum first order reflectivity for the total bilayer thickness d can be calculated using the refraction corrected Bragg's law [3]:

$$\lambda = 2d \sin\varphi \times (1 - 4\bar{\delta} d^2/\lambda^2)\,, \qquad (1)$$

where λ denotes the wavelength, φ is the angle of incidence measured from the surface and $\bar{\delta}$ is the bilayer weighted real part of the refractive index ($n = 1 - \delta + i\beta$). For EUV lithography at 13.5 nm, the material combination of Mo/Si provides the record EUV reflectivity of about 70 % under normal incidence.

2. EUV Light Sources

EUV and soft X-ray light sources can be divided in two classes of large-scale and laboratory-based light sources (Tab. 1). In this chapter, we will shortly review the basic operation principles of a synchrotron, a free-electron laser (both large-scale) as well as the operation principle of an X-ray tube.

Synchtrotron

Synchrotron radiation is generated in an electron/positron storage ring by accelerating relativistic electrons/positrons through a sequence of permanent magnets [4]. There are three types of magnetic structures commonly used to produce synchrotron radiation: bending magnets (2. generation synchrotrons, Fig. 6(a)), as well as undulators and wigglers (3. generation synchrotrons, Fig. 6(b)). The bending magnet radiation has a broad radiation spectrum with a small emission angle (typically $1/\gamma$ half angle), where $\gamma = E/(m_0\, c^2)$ is the Lorentz contraction factor, E is the electron beam energy (typically few GeV's), m_0 the electron mass and c the vacuum speed of light [4]. A wiggler and an undulator are periodic magnetic dipoles with alternating direction of the magnetic field (Fig. 6 (b)).

Large-scale	Laboratory-based
	X-ray tube
Synchrotron	X-ray/EUV laser
Free-electron laser	Laser high harmonics
	Laser-/Discharge-produced plasma

Table 1. Large-scale and laboratory-based EUV and soft X-ray light sources.

The difference between both is that in a wiggler, the deflection angle of the electrons per dipole is larger than $1/\gamma$, whereas in an undulator, the deflection angle of the electrons per dipole is smaller than $1/\gamma$. In the undulator, the electrons and photons have almost the speed of light, but the electron has a slightly longer path compared to the photon. If the path difference equals to the emitted wavelength, there is a coherent superposition of light created by the same electron, which results in emission of so-called undulator harmonics [4].

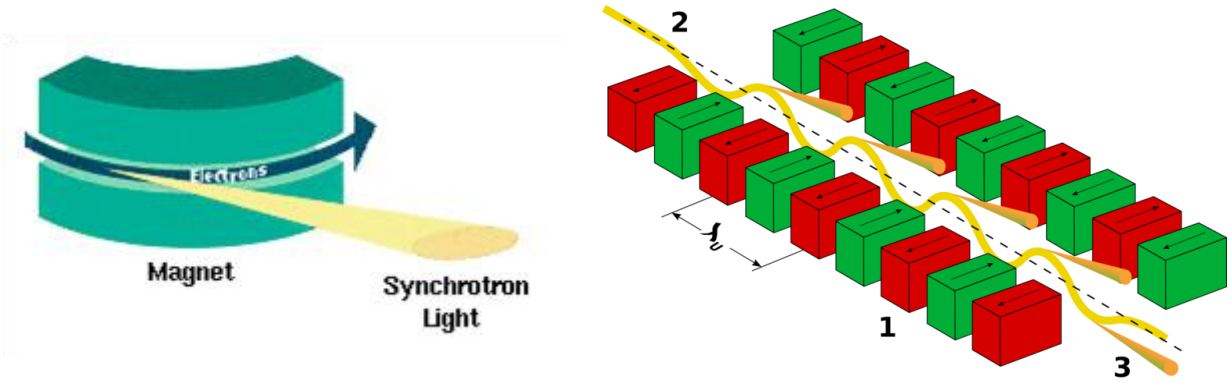

a b

Figure 4. a. Synchrotron radiation from a bending magnet. b. Synchrotron radiation from an undulator [5].

Free-electron laser

A free-electron laser (FEL) consists of a linear electron accelerator and an undulator [6]. In a conventional undulator, there is no correlation between the electron positions. Consequently, electrons emit spontaneous emission, where the emitted intensity is proportional to the number of electrons. In an FEL, the situation is different. Traveling in the undulator nearly at the speed of light, electrons interact with X-rays emitted by other electrons, which changes their energy at the length scale of the X-ray wavelength. Subsequently, moving through the magnetic field of the undulator, electrons are grouped in planes parallel to the propagation direction (Fig. 7 (a)). The distance between the planes is about the X-ray wavelength. The ordered electrons coherently emit X-ray radiation, which amplifies the electron bunching even more. This process is called self-amplified spontaneous emission (SASE) and results in emitted intensity being proportional to the number of electrons squared. The FEL peak photon flux exceeds the peak photon flux of the undulator by orders of magnitude (Fig. 7 (b)).

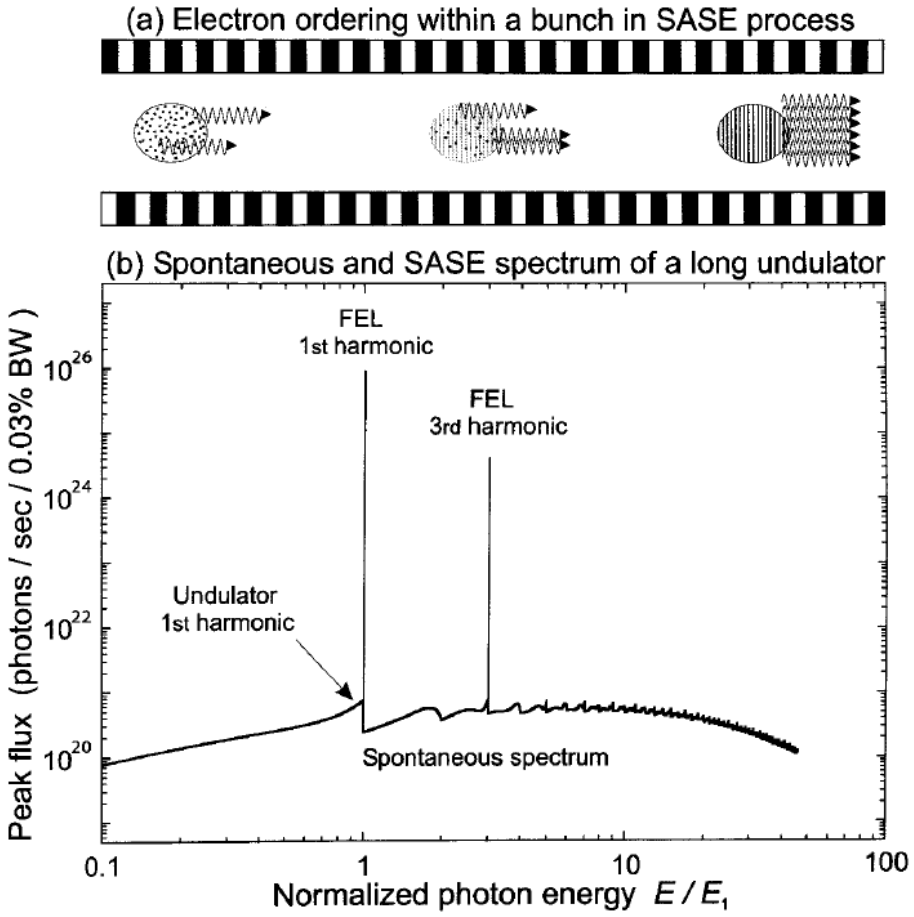

Figure 7. a. Electron ordering within an electron bunch during the process of self-amplified spontaneous emission (SASE). The white and black boxes represent the dipole magnets of the undulator. b. Calculated peak photon flux as a function of photon energy normalized to the photon energy of the first undulator harmonic. The peak photon flux of the first free electron laser (FEL) harmonic is five magnitudes higher compared to the first undulator harmonic [6].

X-ray tube

The simplest version of an X-ray tube consists of a cathode and an anode. The cathode emits electrons, which are accelerated by high voltage (typically tens of kV) and hit the anode. Two possible mechanisms lead to emission of radiation, namely free-free transitions of electrons (Bremsstrahlung) as well as bound-bound transitions of electrons, e.g. from the L to K orbital (K_α radiation), from M to K orbital (K_β radiation), etc. (see Fig. 8). The conversion efficiency (electrical power to radiation power) is about 1%.

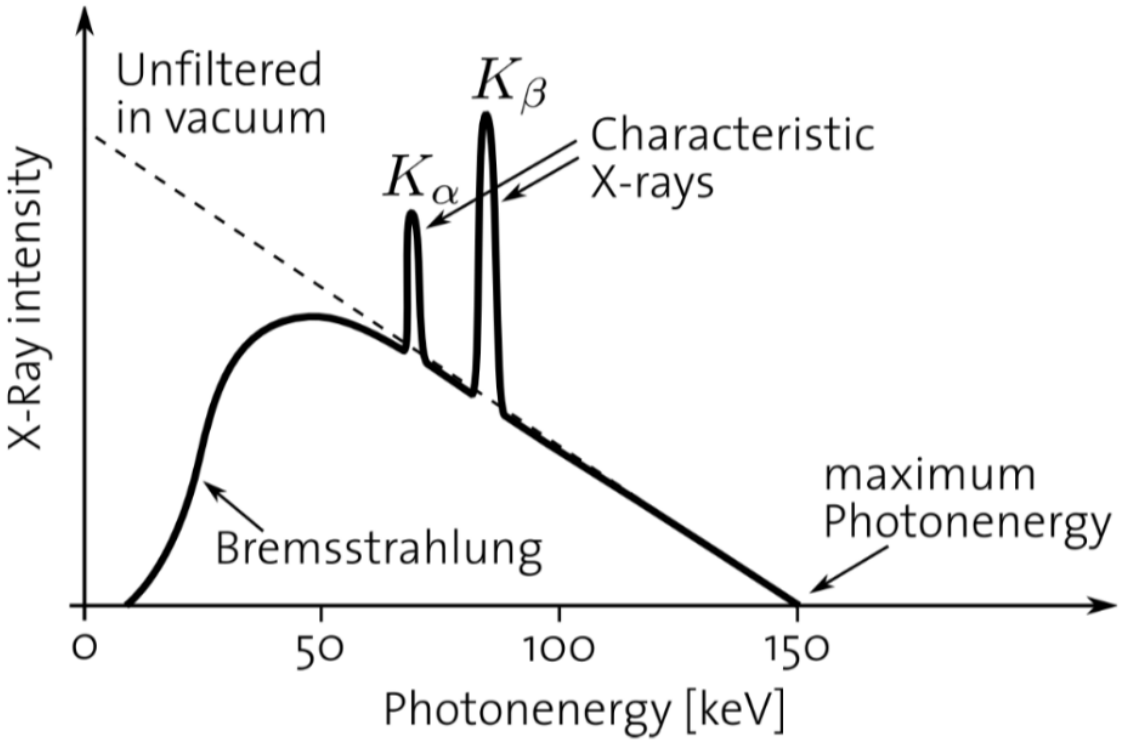

Figure 8. Spectrum produced by an X-ray tube consisting of Bremsstrahlung radiation and characteristic X-ray radiation [7].

3. Plasma and Plasma-based EUV Light Sources

The present experiment uses a hot and dense plasma as a source for EUV radiation. Plasma is one of the four fundamental states of matter (the others being solid, liquid, and gas). Heating a gas may ionize its molecules or atoms (reducing the number of electrons), thus turning it into plasma, which contains charged particles (positively charged ions and negatively charged electrons). Ionization can be induced by other means, such as strong electromagnetic field of a laser or applying an electric field in a gas, where the underlying process is the Townsend avalanche.

Plasmas are highly efficient light sources, e.g. stars, lightings, arc discharges, etc. The total emitted radiation power P_{rad} is contributed mostly by the Bremsstrahlung radiation, P_{br}, recombination radiation, P_{rec}, and spectral line emission, P_{line}, and can be expressed as:

$$P_{rad} = P_{line} + P_{rec} + P_{br}. \quad (2)$$

The contributions are:

- Bremsstrahlung: Radiation is emitted by the free electrons that are decelerated in the Coulomb field of ions. It is a free-to-free electronic transition. Bremsstrahlung has a continuous spectrum.
- Recombination radiation: Free electrons recombining with ions emit the binding energy as light. Due to the free-to-bound electronic transitions, this radiation has a continuous spectrum.
- Spectral line radiation: Electrons bound to ions or atoms can be excited in the plasma to higher energy bound states. The energy for this process is provided by collisions between plasma constituents or by light absorption. This energy is released in a form of radiation when the excited electrons relax back to the equilibrium state or other lower lying states. Since the atomic level structure has a discrete character, the radiation spectrum consists of narrow spectral lines in contrast to broadband recombination and Bremsstrahlung spectra.

The contribution of each process to the overall radiation spectra depends on the density, temperature, composition, and lifetime of the plasma.

According to Kirchhoff's law of thermal radiation, the maximal power a body of arbitrary material can radiate is limited by the radiation power of a black body at the same temperature. In this case, the spectral radiance is given by Planck formula:

$$L_\lambda = \frac{2c^2h}{\lambda^5} \cdot \frac{1}{\exp\left(\frac{hc}{k_B T \lambda}\right) - 1} \quad (3)$$

$$L_\lambda: Spectral\ radiance, k_B: Boltzmann\ constant, \lambda: Wavelength$$
$$c: Light\ velocity, h: Plank\ constant, T: Absolute\ temperature.$$

Applying Wien's displacement law,

$$\lambda \cdot T = const. = 2.898 \cdot 10^{-3}\ m\ K = 250\ nm\ eV,$$

which relates the black body temperature to the wavelength corresponding to the radiance maximum, results in 18.5 eV temperature required for observing the peak of radiance at $\lambda = 13.5$ nm.

The plasma temperature defines not only the maximal achievable radiance but also the ionic charge distribution and, therefore, the emission spectrum. As an example, let us consider xenon gas as the source fuel. Figure 9 shows a change in ionic charge distribution at different temperatures. The emission in the EUV spectral range is contributed mostly by line emission of XeXI (Xe^{10+}, when 10 electrons are stripped from Xe-atom). In order to generate high abundance of these ions in the plasma, the temperature must achieve several tens of electron-volts.

In hot and dense plasmas, the sharp emission lines are Doppler and Stark broadend, due to the motion of emitting ions and collisions between ions and electrons. In addition, particularly in the case of heavy elements (with correspondingly complex electronic strucutre), the spectrum is broadened by the amount of possible transitions. For example, there are about 500 energy levels with about 80,000 transitions between the 5 most common electron configurations and the ground state of XeXI [8].

Another important parameter is the plasma density. For low densities, the radiance of the plasma increases linearly with the density until the collision rate between electrons and ions becomes comparable to the relaxation rate of ionic excited states. Above this limit, the radiance becomes independent of the density since the excited state populations reach thermodynamic equilibrium. Thus, the radiance approaches the blackbody limit [8].

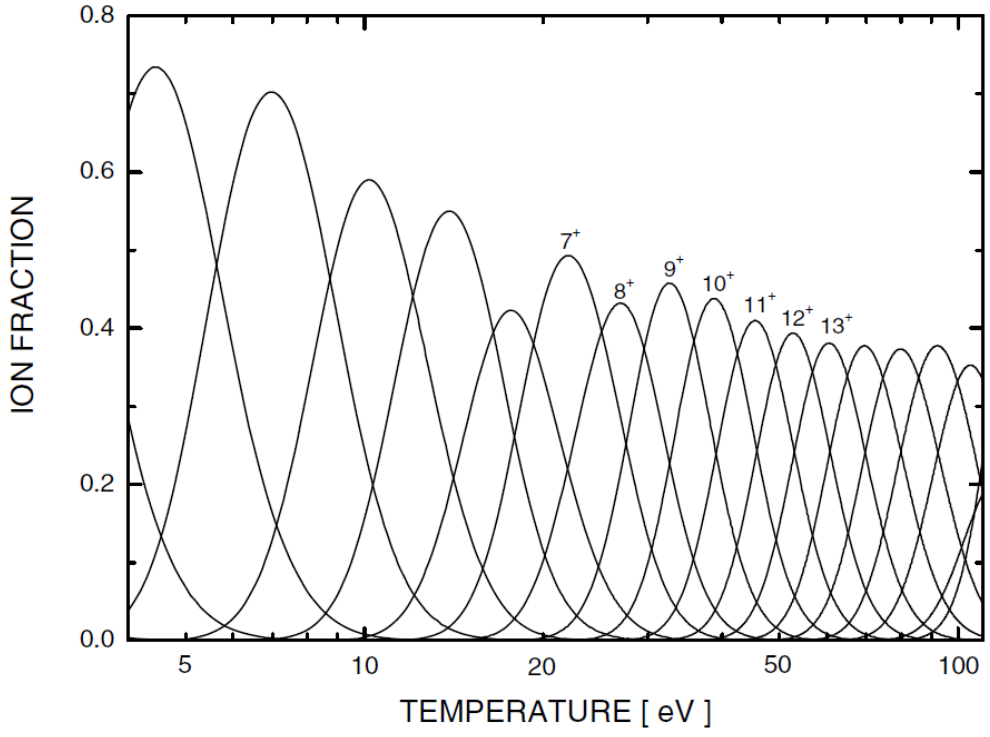

Figure 9. Ionization balance for xenon as a function of electron temperature for $n_e = 10^{19} \frac{1}{cm^3}$ [3].

3.1 Plasma EUV Light Sources

Discharge-produced plasma (DPP) and laser-produced plasma (LPP) are the leading technologies for generating high-power EUV radiation at 13.5 nm. In both technologies, hot plasma of ≈ 20 – 50 eV of the chosen fuel material is generated, which produces EUV radiation (see Table 2). In DPP, magnetic pinching of low-temperature plasma generates high-temperature plasma. In LPP, the target material is heated by a laser pulse to generate high-temperature plasma. Xenon and tin are the most popular fuel materials for EUV sources in the environment of EUV lithography.

Laser Produced Plasma (LPP)

In **LPPs** the Inverse Bremsstrahlung mechanism is utilized to transfer energy from the incident laser radiation to the plasma. An intense pulsed laser beam, which is focused onto a fuel substrate, evaporates and ionizes the fuel. The resulting hot plasma radiates and expands rapidly during the laser pulse. Then, after the pulse ends, the plasma continuing its expansion cools down and recombines within several microseconds. Important advantage of LPPs is their small emission spot size leading to high brilliance of LPP sources. Among disadvantages is a fast degradation of the target material, and therefore, special arrangements of the target regeneration are necessary.

Discharge Produced Plasma (DPP)

DPPs involve discharges of gases. A high voltage (typically $1 - 10$ kV) between two electrodes lead to an electrical breakdown of the (low pressure) gas in between. The electrical avalanche effect leads to an ionization of the gas atoms and leads to the generation of plasma. In DPPs, hot plasmas are readily produced by the pinch effect. This term describes the self-confinement of the plasma accompanied by heating of discharges by the magnetic field of the current. Pinching starts when the magnetic field pressure exceeds the plasma particle pressure, and it stops when the two are equal; this condition describes a magnetically confined plasma column. DPPs mostly differ in electrode design, which controls the dimension, stability and location of the plasma. Advantages of DPP compared to LPPs are lower debris production, higher possible ionization states and lower overall cost. Even though the electrode is not consumed like the target in LPP, its degradation is a weak spot of the DPP concept.

Parameter		LPP	DPP
Pulse duration	ns	0.1 – 50	10 – 1000
Laser/Electrical energy	J/pulse	0.1 – 1.5	2 – 20
Size of the emission zone	µm	50 – 300	100 – 1000
Max. repetition rate	kHz	50	5

Table 2. Comparison of parameters of laser and discharge produced plasmas.

3.2 Hollow-Cathode-Triggered Gas Discharge

The present lab experiment uses a hollow-cathode-triggered (HCT) pinch plasma source to create EUV radiation. Schematic of the setup is shown in Figure 10. This DPP-type source consists of a charging circuit, a capacitor array, and an electrode chamber filled with the fuel gas. Below, four phases of the source operation are described in detail, which are the gas breakdown initiation (dark current) phase, the hollow cathode discharge phase, the plasma pinching phase, and the plasma recombination phase.

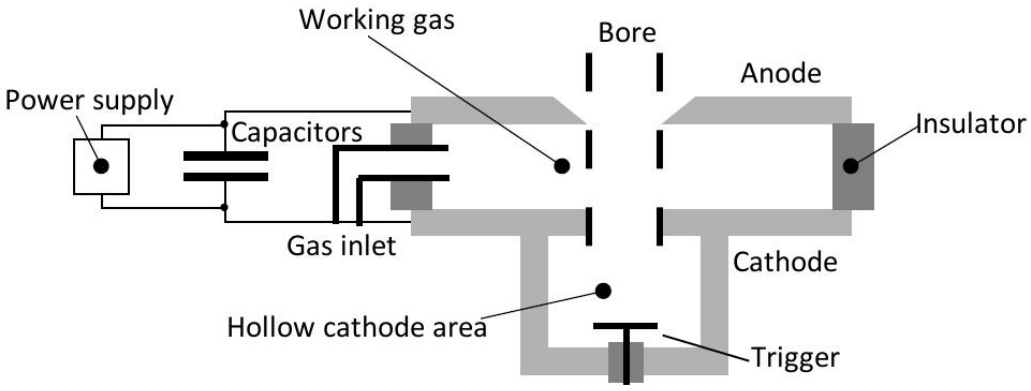

Figure 10. Electrode design of the hollow-cathode-triggered EUV light source [9].

Dark current phase

During initial stages of the discharge, when a voltage drop is initiated between two electrodes in gaseous atmosphere, the Townsend current starts flowing between the electrodes due to natural abundance of free charges in the gas. This current leads to avalanche ionization of the gas. In the described device, the electrode geometry and gas pressure are chosen such that this avalanche ionization occurs only at the edges of the electrode bore hole.[1] The Paschen curve in Figure 11 illustrates this effect. This curve relates the gas breakdown voltage to the inter-electrode distance *d*, the pressure of the fuel gas *p,* and the material constant of the working gas. The gas pressure in the inter-electrode region is selected such that the source is operated in the left-hand part of the Paschen curve (the breakdown voltage drops with the increase of the *p·d* product), to maximize the breakdown voltage. The breakdown starts at the edges of the bore hole, where the effective inter-electrode distance is larger than everywhere else leading to larger *p·d* product, and therefore, to lower breakdown threshold compared to other locations. This is essential for generating plasma in the bore region, from which the plasma radiation can be effectively collected during the pinching phase.

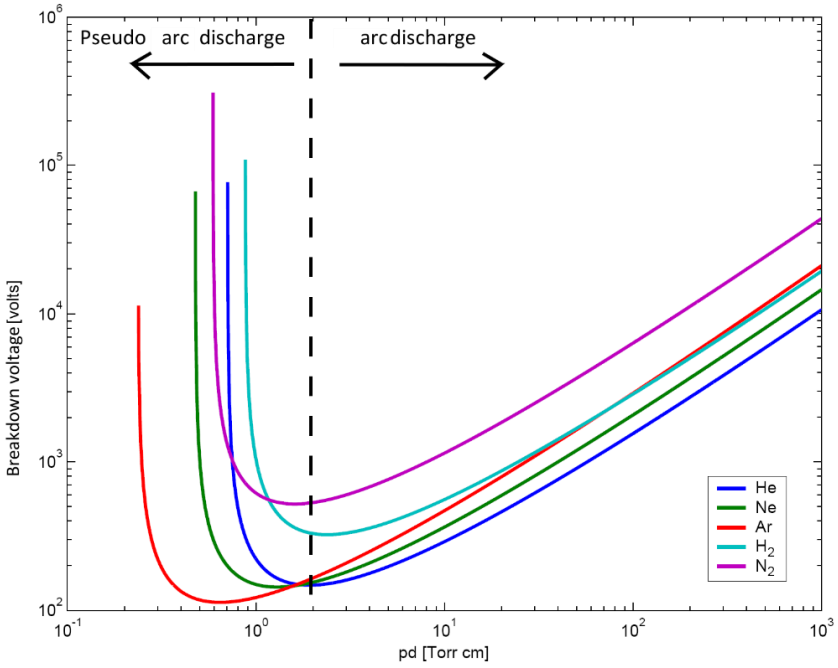

Figure 11. The Paschen curve shows the minimal voltage needed to create an electrical breakdown between two electrodes as a function of the pressure p and electrode distance d for different gases [10].

[1] As the charged particles follow the electrical field, which is bend at the edge of the electrodes, their effective travel distance increases. The electrodes are close (~mm) and the pressure is low (1 – 100 Pa), and therefore, only at the edges of the bore the traveling distance of the electrons is long enough to produce an ignition.

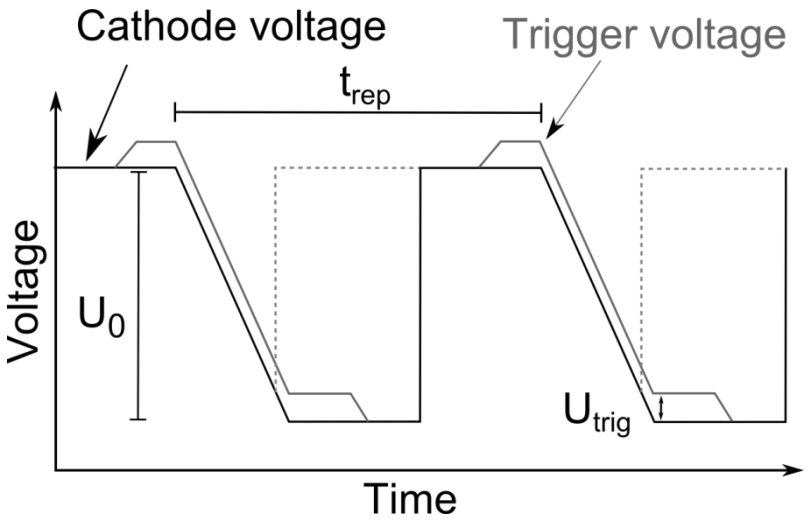

Figure 12. Time-dependent voltage at the cathode and at the trigger of the DPP source. The dotted lines indicate the discharge characteristic if no trigger is used. The slope and shape of the charging curve depends on the used power supply [9].

Hollow cathode phase

In order to enhance and stabilize the initial discharge, a special geometry of the cathode electrode is employed – the so-called "hollow cathode". Behind the bore drilled through the cathode, an additional enclosed compartment filled with the same gas is attached (see Figure 10). Due to a negative charge of the compartment walls, they attract ions from the inter-electrode gap. These ions striking the walls produce secondary electrons that accelerate back to the bore region. Before reaching the bore, the secondary electrons may bounce between the hollow cathode walls ionizing the fuel gas on the way. This effect enhances substantially the breakdown process.[2] Furthermore, ignition can be prevented, when an additional electrode is added to the hollow cathode chamber. Applying a slightly higher potential than at the surrounding cathode, it collects the free electrons preventing plasma ignition until the trigger potential is set to the potential at the cathode (Fig. 12).

Pinch plasma phase

After the gas breakdown is initiated (requires several tenths of nanoseconds), a highly conductive plasma column bridges the electrodes in the bore space. The charge accumulated in the capacitor bank begins to flow through the plasma and generates a pulse of a high current (typically ~10 kA). The strong magnetic field of the current interacts with the charged particles of the plasma through the Lorentz force and compresses the plasma column towards the axis of the bore. Due to the rapidly

[2] This effect is so strong that it enables to control the ignition time with the size of the compartment and/or with an additional triggering electrode in the compartment.

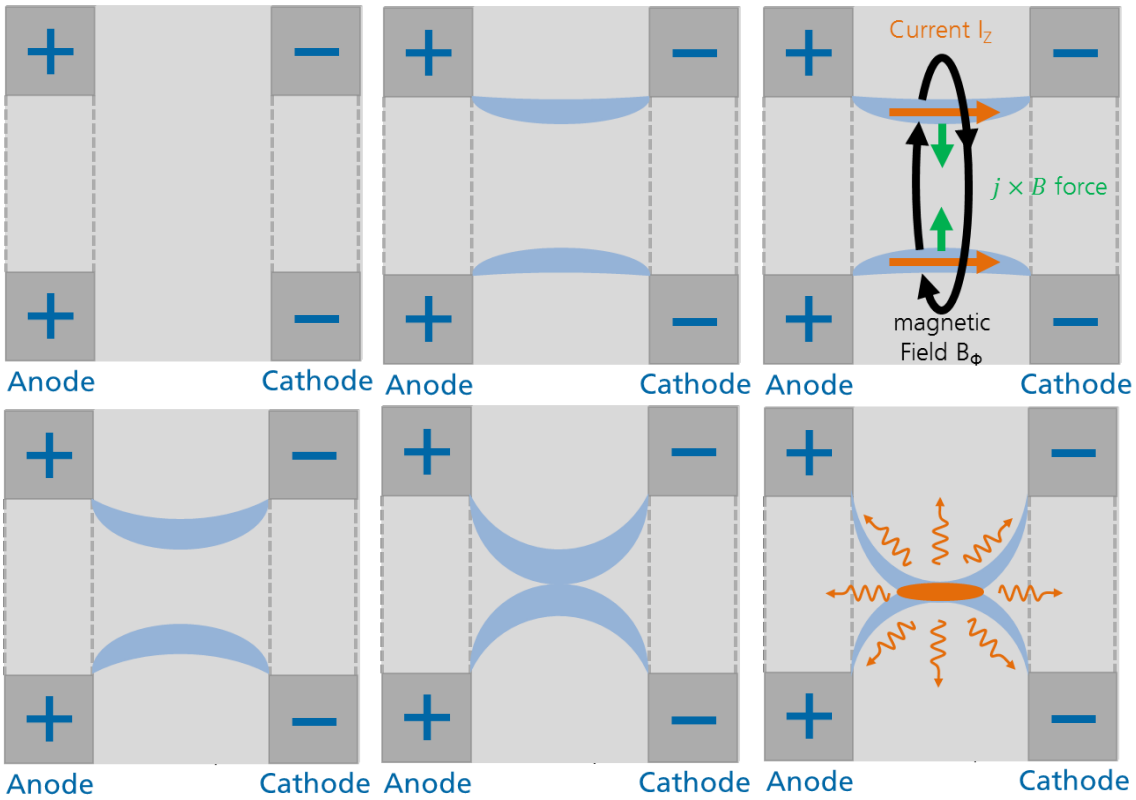

Figure 13. Pinching of the plasma by its self-induced magnetic field.

changing current (and the magnetic field) and high conductivity of the plasma, the diffusion of the plasma particles across the magnetic field is suppressed (skin-effect). The latter leads to dramatic reduction of the volume occupied by the plasma during the compression and, therefore, to the increase of the plasma density and temperature necessary to generate EUV radiation. In particular, in the present setup, the current pulse of 200 ns duration peaks at 8 kA and generates a magnetic field of up to 4T, which compresses a 2.5 mm diameter plasma column to 0.5 mm. This plasma compression process is called pinch effect illustrated in Figure 13. The compression stops, when the magnetic pressure is balanced by dynamic pressure of plasma particles. The resulting temperature, density, and column radius can be approximated using the Bennett relation [11]:

$$\frac{\mu_0 I_0^2}{8\,\pi^2\, r_p^2} = (n_i + n_e) k T_e \,. \qquad (4)$$

Assuming tenfold ionization, $n_e = 10\, n_i$, a starting pressure of $p = 10$ Pa and a starting radius of $a = 2.5$ mm, this gives an estimate of $T_e = 35$ eV for the electron temperature taking $r_p = 0.5$ mm, $n_e = 10^{18}$ cm^{-3}, and the peak current of $I = 8$ kA. The plasma under these conditions is an effective emitter of the EUV radiation.

Recharge and recombination phase

Upon completion of the capacitor bank discharge, the current stops flowing through the plasma, and the magnetic field pressure drops to zero. Because the dynamic pressure of the plasma is not balanced anymore by the magnetic field pressure, the plasma begins expanding freely (at the speed of about 4000 m/s) into the inter-electrode space hitting eventually the walls and recombining. This process may take up to several hundreds of microseconds depending on fuel gas and geometry of the electrodes (in particular of the hollow cathode compartment where the charged particles need longer to diffuse to the walls). This time limits, together with the recharging time of the capacitors, the repetition rate of the DPP-source, since the requirements for optimal source performance dictate that every discharge pulse must begin at the same initial state of the fuel gas in the inter-electrode space. Another limit for the repetition rate is the cooling of the electrode system. Increasing the repetition time needs sophisticated cooling concepts. Without any additional cooling the repetition rate is limited to a few tens of Hz.

Conversion efficiency

The electrical energy stored in the capacitor bank of the source is coupled into the plasma during the discharge and pinching phases. This energy is converted into the particle motion energy and also into energy of radiation. Due to the complex radiation mechanisms described above, the spectrum of plasma radiation spans from far infrared to X-ray spectral regions. A figure of merit for optimization of the source is the conversion efficiency factor η_{CE}:

$$P_{\Delta\lambda} = f \cdot E_{\Delta\lambda} = f \cdot \eta_{CE} \cdot E_C \,, \tag{5}$$

$$P_{\Delta\lambda}\ and\ E_{\Delta\lambda}: In-band\ radiation\ power\ and\ energy,$$
$$f: Repetition\ rate, E_C: Electrical\ energy,$$

which is a ratio between average radiation power emitted into the spectral region of interest $P_{\Delta\lambda}$ and the average electrical power to maintain the repeated discharge. Typical values of the conversion efficiency factor are around $\eta_{CE} \sim 0.2\,\%$ into the bandwidth of ± 0.135 nm around $\lambda = 13.5$ nm for sources operating in low-kHz repetition rate range. For generation of e.g. 100 W of the average radiation power, one needs around 50 kW average electrical power. Figure 14 illustrates the power

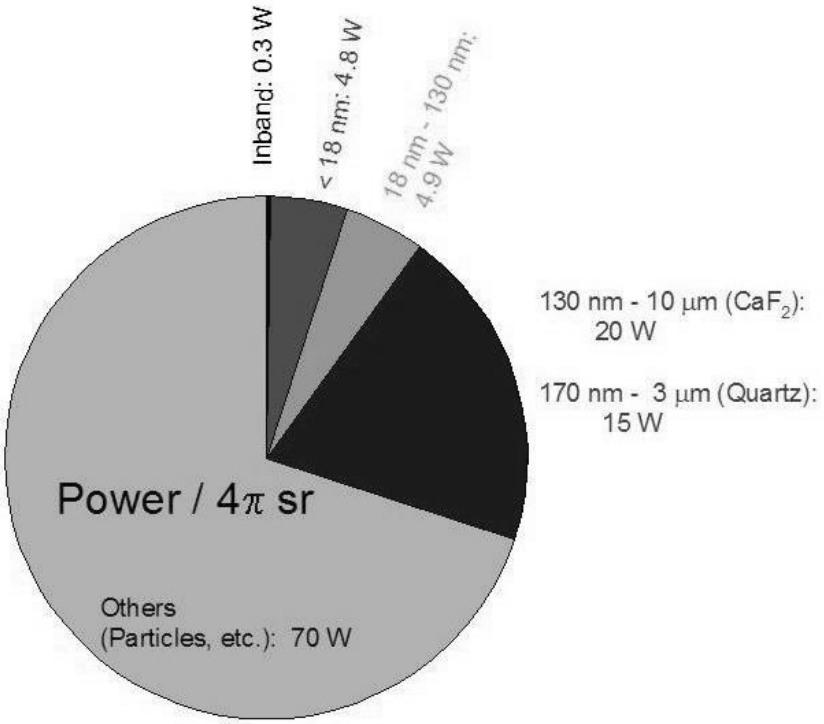

Figure 6. Pie chart for the power distribution of a DPP EUV light source operating with Xe gas [12].

distribution in the plasma. The conversion efficiency can be optimized by changing the electrode geometry, discharge parameters and the fuel gas.

4 EUV Metrology and Lab Course Procedure

4.1 EUV Metrology

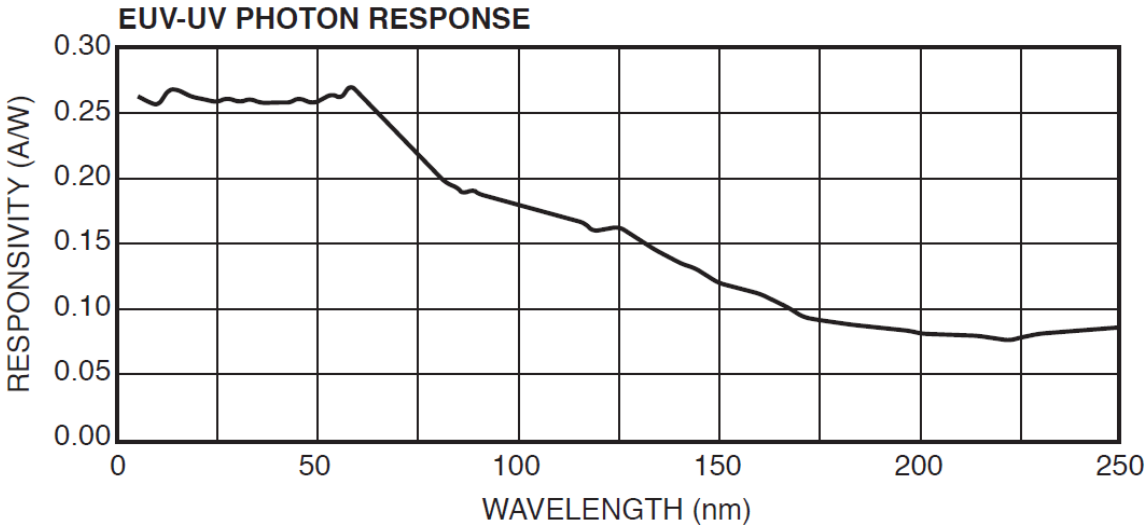

Figure 7. Responsivity of the AXUV 100G photodiode used in the energy monitor.

Photodiode

For measurements of the energy per pulse within a certain region of EUV spectrum reflected by the Bragg mirror, we use a calibrated Si photodiode sensitive to EUV radiation (AXUV 100G from Opto Diode Corp.). When the photodiode is exposed to photons of energy greater than 1.12 eV (wavelength less than 1100 nm) electron-hole pairs (carriers) are created. These photo-generated carriers are separated by the electric field of the p-n junction and a current proportional to the number of created electron-hole pairs flows through an external electric circuit. The current pulse is measured indirectly as a voltage pulse on the oscilloscope. For EUV photons, it effectively takes 3.7 eV to generate one electron-hole pair. Therefore, many electron-hole pairs are created by one photon. This results in device quantum yield (electrons seen by an external circuit per incident photon) much greater than unity. The photodiodes are also characterized by a spectral responsivity curve (shown in Figure 15). The spectral responsivity is used to convert the measured voltage pulse to the total energy per pulse of EUV radiation incident onto the photodiode.

CCD detector

A CCD-camera (charge-coupled device) is a detector, which allows measurements of spatial distribution of light intensity. A single pixel of CCD consists of p-doped Si substrate covered with layers of SiO_2 and polycrystalline Si forming the gate electrode. The positively biased gate creates a potential well, where electrons are confined. Electron-hole pairs are created by incident photons by means of the internal

photoelectric effect. The positively charged holes are drifting away, whereas the electrons are trapped in the potential well of the gate. The number of photo-generated electrons is proportional to the intensity of the incident radiation. A shift register enables the readout of each single pixel. Thus, the detector gains spatial resolution. Due to the high absorption in the EUV spectral range, the conventional CCD detector has to be modified. Otherwise, the incident EUV radiation will be mostly absorbed in the polycrystalline Si and SiO_2. Figure 16 illustrates two concepts allowing for increasing the sensitivity of the CCD detector in the EUV spectral region. One possibility is to deposit a layer of scintillating material (e.g. Tb-doped Gd_2O_2S) on top of the gate in order to convert the EUV radiation into visible light, which penetrates into the Si and generates electron-hole pairs. Alternatively, the backside of the Si substrate is etched all the way down to the photosensitive region, and the EUV radiation is directed to the CCD from the backside. This type of CCD detector (e.g. Andor iKon M, 1024 pixel x 1024 pixel, 13 µm pixel size) is used in the present lab course. Advantages of CCD cameras compared to standard CMOS-based cameras are their low read-out noise, high uniformity and sensitivity. To decrease the (dark) noise even more, the CCD can be additionally cooled.

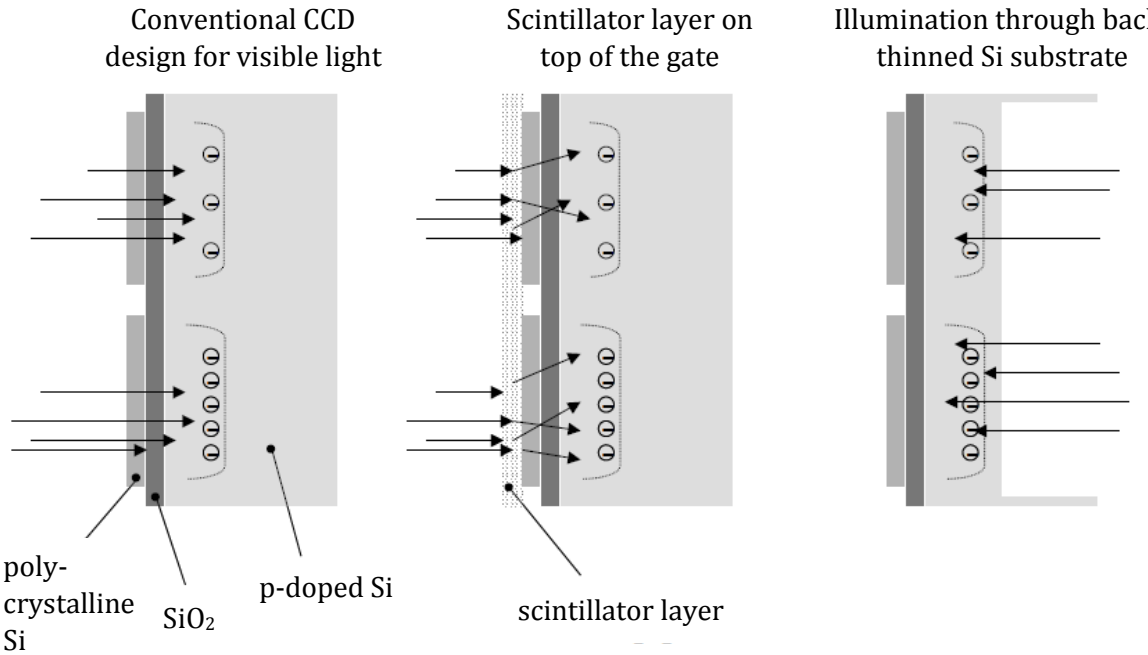

Figure 8. The layer structure of a charge-coupled device (CCD). In the visible spectral range, the light penetrates through the layers of polycrystalline Si and SiO_2 to the photosensitive region of p-doped Si and generates electron-hole pairs (left). Due to the high absorption in the EUV spectral range, the CCD has to be modified in order to efficiently detect EUV radiation. Either a scintillator layer is deposited on top of the gate (middle) or the EUV radiation illuminates the detector from the backside of the etched Si substrate (right).

In-band energy monitor

To determine the average in-band EUV power of the pulsed light source, i.e. the power emitted within a defined spectral region, it is required to determine the in-band energy per pulse. In our lab course, we will determine the energy per pulse around 16.5 nm (xenon gas) and around 17.3 nm central wavelength (oxygen).

The energy monitor consists of a a ([Si(8.04 nm)/B_4C(5.36 nm)]$_{50x}$ on Si) multilayer mirror and a photodiode (AXUV 100G from Opto Diode Corp.). The signal is monitored on the oscilloscope. The emission of the gas-discharge plasma light source ranges from infrared to the soft x-ray spectral region and includes EUV radiation. In order to suppress wavelengths above 80 nm and between 5 nm and 17 nm we use an Al filter (200 nm thickness). In the next steps, we will derive the important expression which connects the energy per pulse and solid angle $E_{\Delta\lambda}$ for a wavelength region between $\lambda_0 - \Delta\lambda/2$ and $\lambda_0 + \Delta\lambda/2$ around λ_0, the voltage pulse from the photodiode and the parameters of the energy monitor. We start with the general expression

$$\int_0^\infty \mathrm{d}\lambda\, S(\lambda) T_{gas}(\lambda) R(\lambda) T_{filter}(\lambda) D_{diode}(\lambda) = \frac{1}{\Delta\Omega R_{scope}} \int_0^{t_P} \mathrm{d}t\, U_{diode}\,(t)\,, \qquad (5)$$

where, on the left side, $S(\lambda)$ denotes the spectral energy per pulse and solid angle (in J/(sr ·m)), $T_{gas}(\lambda)$ denotes the transmission of the gas between the source and the photodiode, $R(\lambda)$ is the reflectivity of the multilayer mirror, $T_{filter}(\lambda)$ is the filter transmission and $D_{diode}(\lambda)$ denotes the photodiode responsivity (in A/W, for AXUV 100G photodiode see Fig. 15). On the left side, $\Delta\Omega$ is the solid angle, R_{scope} denotes the resistance of the oscilloscope, $U_{diode}\,(t)$ is the voltage pulse from the photodiode and t_P the pulse duration.

First, we approximate $T_{gas}(\lambda) = T_{gas} = \text{const.}$, i.e. the gas transmission is wavelength independent. Then we define the sensitivity of the energy monitor

$$D_{tool}(\lambda) = R(\lambda) T_{filter}(\lambda) D_{diode}(\lambda) \qquad (6)$$

and also normalize $S(\lambda)$according to the equation

$$S(\lambda) = S_0 \cdot \tau(\lambda)\,,$$

where $\int_0^\infty \mathrm{d}\lambda\, \tau(\lambda) = 1$. For the energy per pulse and solid angle $E_{\Delta\lambda}$ between $\lambda_0 - \Delta\lambda/2$ and $\lambda_0 + \Delta\lambda/2$ around λ_0 we can write

$$E_{\Delta\lambda} = S_0 \int_{\lambda_0-\Delta\lambda/2}^{\lambda_0+\Delta\lambda/2} \mathrm{d}\lambda\, \tau(\lambda) = \frac{S_0 \int_{\lambda_0-\Delta\lambda/2}^{\lambda_0+\Delta\lambda/2} \mathrm{d}\lambda\, \tau(\lambda) \cdot \frac{1}{\Delta\Omega R_{scope} T_{gas}} \int_0^{t_P} \mathrm{d}t\, U_{diode}\,(t)}{S_0 \int_0^\infty \mathrm{d}\lambda\, \tau(\lambda)\, D_{tool}(\lambda)}.$$

Finally, we can define the energy monitor calibration factor

$$\chi = \frac{\int_0^\infty \mathrm{d}\lambda\, \tau(\lambda)\, D_{tool}(\lambda)}{\int_{\lambda_0-\Delta\lambda/2}^{\lambda_0+\Delta\lambda/2} \mathrm{d}\lambda\, \tau(\lambda)}$$

and write

$$E_{\Delta\lambda} = \frac{1}{\chi} \cdot \frac{1}{\Delta\Omega R_{scope} T_{gas}} \int_0^{t_P} \mathrm{d}t\, U_{diode}\,(t)\,. \qquad (7)$$

In practice, the a priori knowledge of $\tau(\lambda)$, and therefore, of the spectral distribution is necessary to determine $E_{\Delta\lambda}$. In our case, $\tau(\lambda)$ can be written as a sum of weighted Dirac delta functions with weighting factors a_i

$$\tau(\lambda) = \sum_i a_i \cdot \delta\,(\lambda - \lambda_i\,)$$

due to the very narrow bandwidth of spectral lines $\left(\frac{\Delta\lambda}{\lambda} = 10^{-3} - 10^{-4}\right)$. Consequently, χ can be written as

$$\chi = \frac{\int_0^\infty \mathrm{d}\lambda \sum_i a_i \cdot \delta\,(\lambda - \lambda_i\,)\, D_{tool}(\lambda)}{\int_{\lambda_0 - \Delta\lambda/2}^{\lambda_0 + \Delta\lambda/2} \mathrm{d}\lambda \sum_j a_j \cdot \delta\,(\lambda - \lambda_i\,)} = \frac{\sum_i a_i \cdot D_{tool}(\lambda_i)}{\sum_j a_j}\ . \tag{8}$$

It has to be noted that the weighting factors a_i with index i have to be taken for the whole spectrum, whereas the weighting factors a_j with index j have to be taken only between $\lambda_0 - \Delta\lambda/2$ and $\lambda_0 + \Delta\lambda/2$.

In our case, we are interested in $E_{\Delta\lambda}$ around $\lambda_0 = 16.5$ nm (xenon gas) and $\lambda_0 = 17.3$ nm (oxygen gas) nm. Parameters to determine $E_{\Delta\lambda}$ from lab course measurements are summarized in Tab. 3.

Parameter	Reference/Measurement
$\boldsymbol{R}(\lambda)$of the multilayer mirror ([Si(8.04 nm)/B4C(5.36 nm)]$_{50x}$ on SiO_2 angle of grazing incidence 41.6° / 43.8°	CXRO webpage[3]
T_{filter} of the Al foil (200 nm)	CXRO webpage[4]
D_{diode}	Fig. 15
$T_{gas} \approx 1$	
R_{scope}	adjustable in the experiment
$\Delta\Omega$	to be measured in the experiment
$U_{diode}\,(t)$	to be measured in the experiment

Table 3. Parameters required to determine the energy per pulse and solid angle.

[3] http://henke.lbl.gov/optical_constants/multi2.html
[4] http://henke.lbl.gov/optical_constants/filter2.html

EUV spectrometer

The EUV spectrometer used in the present lab course consists of a slit (50 μm width), a grating on a circular surface (radius of curvature R = 1000 mm) and a CCD detector (see Figure 17 and Table 4). A circle with a radius R/2, which arc intersects the central point of a spherical surface with radius R is called Rowland circle. If an object is placed somewhere on the Rowland circle, it will be imaged with magnification M=1 on another place on the Rowland circle. This imaging property of a spherical surface is employed in the EUV spectrometer to enhance the spectral resolution. For that purpose, the slit is placed on the Rowland circle. For each spectral line, the slit is imaged[5] by the grating on the CCD detector located at the corresponding position on the Rowland circle. If r denotes the distance between the slit and the grating, r' denotes the grating-CCD detector distance, α is the angle of incidence of the beam, and β the angle of diffraction measured with respect to the grating normal, the condition for the slit to be imaged on the CCD detector reads:

$$r = R \cdot \cos(\alpha)$$

$$r' = R \cdot \cos(\beta).$$

For R = 1000 mm and α = 80°, r equals to 174 mm. On the other hand, β depends on the diffracted wavelength, and therefore, r' is also wavelength-dependent. In general, the grating equation reads:

$$m \cdot \lambda = d \cdot (\sin(\alpha) + \sin(\beta)) \quad (9),$$

where λ denotes the wavelength, m=±1,±2,... the diffraction order, and d the grating constant. The angles α and β are measured from the grating normal, and positive angles are defined for counterclockwise rotation and negative angles - for clockwise rotation. In order to avoid any sign confusion, we rewrite the grating equation

$$m \cdot \lambda = d \cdot \{\sin(|\alpha|) - \sin(|\beta|)\}.$$

The CCD detector is positioned at distance z from the grating, and x denotes the position on the chip ($= x_0$ for the specular reflected beam). With the condition

$$\tan(|\alpha| - |\beta|) = \frac{x - x_0}{z}$$

the equation for wavelength calibration reads

$$\lambda(x) = \frac{d}{m} \cdot \left\{\sin(|\alpha|) - \sin\left(|\alpha| - \operatorname{atan}\left(\frac{x - x_0}{z}\right)\right)\right\} . \quad (10)$$

If p denotes the pixel size (p=13 μm in our CCD camera) and n is the pixel number, Eq. (10) can also be written as

$$\lambda(n) = \frac{d}{m} \cdot \left\{\sin(|\alpha|) - \sin\left(|\alpha| - \operatorname{atan}\left(\frac{p(n - n_0)}{z}\right)\right)\right\} . \quad (11)$$

[5] Even more, the shape of the line in direction perpendicular to x (Fig. 17) is a pinhole image of the pinch for this particular wavelength.

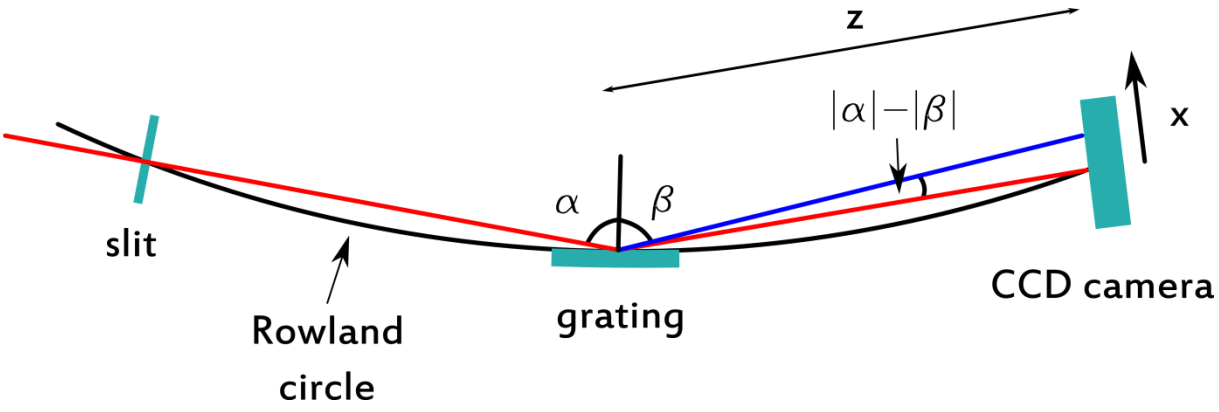

Figure 9. EUV spectrometer used in the lab course. The EUV radiation shines through a thin slit located on the Rowland circle of the spherical grating. The diffracted light is focused at another point of the Rowland circle, where the CCD detector is placed.

grating constant	d=1/1200 mm (1200 lines/mm)
angle of incidence	α=80°
radius	R=1000 mm
ruled area	A=260 mm x 260 mm
blaze angle	γ=2.4°
distance grating-CCD detector	z=250 mm
CCD pixel size	p=13 µm
number of pixel	N=1024

Table 4. Parameters of the EUV spectrometer.

Following parameters determine the spectral resolution $\Delta\lambda$ of the spectrometer:

- grating dispersion $\frac{d\lambda}{dx}$
- slit size
- position of the CCD detector with respect to the Rowland circle
- number of illuminated grooves of the grating
- angular resolution
- imperfections of the grating

The grating dispersion is the first derivative of λ with respect to x (Eq. 10). At 20.5 nm wavelength, $\frac{d\lambda}{dx} = 0.92$ nm/mm. The best spectral resolution is achieved for the wavelength λ_0, which is located at the pixel intersecting with the Rowland circle. If we denote Δx the distance on the CCD detector between λ_0 and the wavelength of consideration λ, the resolution $\Delta\lambda$ is proportional to Δx. Furthermore the wavelength resolution depends on the angular resolution. Here it is important to remember that the EUV plasma light source emits radiation into 2π solid angle (divergent light source) and that the source has a finite size. If we denote W_S the source size perpendicular to the optical axis and D_S the source-slit distance, for the divergence angle φ_D we find:

$$\tan\varphi_D = \frac{W_S}{D_S}$$

Typically, for W_S=750 µm (for O_2 pinch) and D_S=1500 mm, φ_D amounts to $6.7 \cdot 10^{-4}$ rad. Taking all the different contributions into account, the spectral resolution is

$$\Delta\lambda = \frac{d\lambda}{dx} \cdot c_g \Delta x \cdot \tan\varphi_D \ , \qquad (12)$$

where c_g denotes a grating specific factor (c_g=3.9 for our 1200 lines/mm grating). For the parameters given above, $\Delta\lambda \approx 10^{-2}$ nm at λ=20.5 nm.

4.2 Lab Course Procedure

Measurements

1. Measurement of energy-per-pulse at 16.5 nm (xenon gas) and/or at 17.3 nm (oxygen gas) behind the Bragg mirror using a calibrated Si photodiode (AXUV 100G) and an oscilloscope.
2. Measurement of the spectrum with xenon and/or oxygen gas behind the Bragg mirror using an EUV-spectrometer.
3. Measurement of the spectrum with xenon and/or oxygen gas directly behind the EUV light source using an EUV-spectrometer.

Data analysis

Spectra:

Typical raw data from the CCD camera are shown in Fig. 18. Use the NIST Atomic Database [6] (http://physics.nist.gov/PhysRefData/ASD/lines_form.html) to identify the spectral lines. Assign the wavelengths λ from the NIST Atomic Database to the pixel numbers n of the peaks and fit the data using Eq. (11). Please show the calibration plot

[6] You should not only search for the observed lines, but also in the Ritz Wavelengths. The Einstein coefficient will help you to cross out the unlikely ones. The nomenclature follows the rule: Neutral oxygen O I, one-time ionized oxygen: O II, two-times ionized oxygen: OIII, etc.. Another way to extract the spectrum directly is the Saha/LTE-Spectrum. Assume a plasma density of 10^{18} cm^{-3} and use plasma temperatures between 10 and 20 eV.

(pixel vs. wavelength) and the calibrated spectra. If $I_{source}\ (\lambda)$ denotes the spectrum behind the EUV light source and $I_{Bragg}\ (\lambda)$ is the spectrum behind the Bragg mirror, determine the relative spectral reflectivity $R_{rel}\ (\lambda) = I_{Bragg}\ (\lambda)/I_{source}\ (\lambda)$. You can normalize the peak value to 1 and qualitatively compare $R_{rel}\ (\lambda)$ with expected reflectivity of the Bragg mirror from the database of the Center for X-ray Optics (http://henke.lbl.gov/optical_constants/).

Energy-per-pulse:

First, determine the solid angle ΔΩ of the EUV light source. For that purpose, you need to know the area of the limiting (smallest) aperture $A_{Aperture}$ (it can be an aperture in the beam path or the area of the photodiode). If r denotes the distance between the source and the smallest aperture, the solid angle can be calculated according to equation

$$\Delta\Omega = \frac{A_{Aperture}}{r^2}\ . \qquad (13)$$

Determine the energy-per-pulse using Eq. (6) - (8). Please provide results for a_i, $D_{tool}(\lambda)$ χ, $\Delta\Omega$, the integral $\int_0^{t_P} \mathrm{d}t\ U_{diode}\ (t)$ and $E_{\Delta\lambda}$. Calculate also the ratio between the energy per pulse and the electrical discharge energy (C=0.875 µF, U=2.2 kV) (conversion efficiency (Eq. 5)).

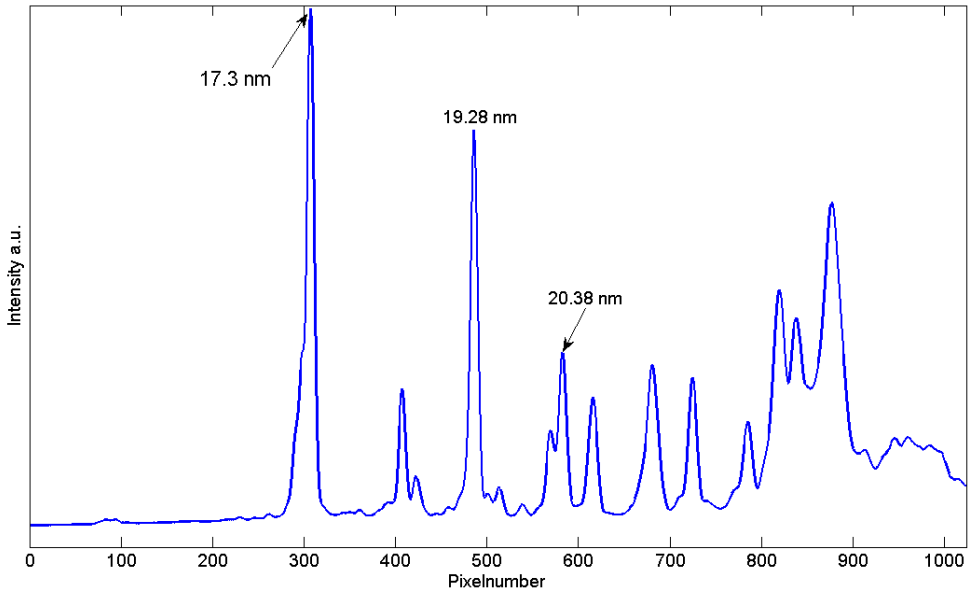

Figure 18. Emission spectra of an oxygen plasma after transmission through an aluminum filter. Characteristic emission lines are indicated by arrows.

5. References

[1] D. Attwood, Soft X-rays and Extreme Ultraviolet Radiation, Cambridge University Press (1999)

[2] C. Wagner, and N. Harned, Nature Photonics 4, 24 (2010)

[3] L. Juschkin, G. Derra and K. Bergmann, EUV Light Sources in 'Low Temperature Plasmas. Fundamentals, Technologies, and Techniques', Chapter 24, Wiley-VCH Verlag (2008)

[4] X-Ray Data Booklet, Center for X-ray Optics and Advanced Light Source, Berkeley, USA, 2009 (http://xdb.lbl.gov/xdb-new.pdf)

[5] http://en.wikipedia.org/wiki/Synchrotron_radiation

[6] J. Stöhr, and H. C. Siegmann, Magnetism, Springer (2006)

[7] http://people.ee.ethz.ch/~cattin/MIA-ETH/pdf/MIA-01-Modalities1.pdf

[8] T. Krücken, K. Bergmann, L. Juschkin, and R. Lebert, J. Phys. D: Appl. Phys. 37, 3213 (2004)

[9] O. Rosier, ‚Pinchplasma mit Hohlkathodenzündung als Strahlungsquelle im extremen Ultraviolett', PhD Thesis (2004)

[10] http://en.wikipedia.org/wiki/Paschen%27s_law

[11] N.A. Krall, and A.W. Trivelpiece, Principle of Plasma Physics, San Francisco Press, (1986)

[12] T. Misalla et al., Proceedings of SPIE 5374, 979 (2004)